To be published as a chapter of the book "Multiscaling in Fracture Mechanics" edited by G. C. Sih, Springer

Ductile Cr-Alloys with Solute and Precipitate Softening

S. Hao and J. Weertman
Department of Material Science & Engineering
Department of Mechanical Engineering
Northwestern University, Evanston, IL 60208, U. S. A.

Abstract
A dislocation kinetics-based analysis has been performed to investigate toughening mechanisms of alloys. It is concluded that strength and toughening are determined by the combination of short range material adhesion and long range interaction between different phases, where the former refers to Peierls-Nabarro energy barrier and coherence embedded solute elements and the latter refers to the double kink formation of dislocation loops and associated pattern of slip line between dispersed solute atoms, precipitates, and second phase particles. A strategy for toughening alloys is proposed that contains two key elements: 1. Alloy softening through smeared out Peierls-Nabarro stress barriers. 2. Process-structure optimization to obtain desirable grain size, coherency and spacing between solutes, precipitates, and second phase of particles.

Keywords: dislocation; double-kink formation; ductile fracture; alloy softening; Cr-based alloy; Peierls-Nabarrostress

1. Introduction
Cr is a promising base for alloy system due to its high melting temperature, high thermal conductivity with moderate strength, low density and low cost. On the other hand, a significant drawback of Cr, as compared with, for example, Fe-Ni-based alloys, is its high ductile-to-brittle transition temperature (about 150^{o}C for unalloyed Cr). It presents a purely brittle behavior at room temperature that hampers effective applications for many engineering purposes. Although many research reports have been published about this class of alloys in recent years, a challenge remains in finding a Cr-based system with acceptable ductility. This paper is a part of a broad study [1] for developing a new class of Cr-based alloys with high strength and high toughness. In particular, we examine the alloy softening mechanism [2-5] as way of achieving increased toughening.

In contrast to cleavage fracture, ductility is deformation of metal by easy movement of crystal dislocations across certain slip systems. The barrier against easy movement of a crystal dislocation is a large amplitude Peierls-Nabarro periodic stress. The surmounting of the Peierls-Nabarro barrier by a straight dislocation occurs by the intermediate step of throwing a double kink over the barrier [6]. In order to identify the double kink formation in semi-conduct materials, Celli, et. al [7] and Guyot & Dorn [8] studied the theoretical solution for the motion of dislocation line under an applied stress.

Urakami and Fine have investigated the dislocation double kink formation in Mg-based alloys with Li addition [5, 9] and Sato and Meshii in iron [10]. The analysis below is an investigation of the condition for double kink formation in a metal with misfit second phase particles which combines a semi-analytical dislocation solution and the results of ab initio computations [11, 12].

This paper is organized as follows: Section 2 introduces the models and associated governing equations. The section that follows introduces a micro-mechanical analysis of particle misfit. Section 4 presents results of a semi-analytical solution of double kink formation. Discussion and conclusions are given in Section 5.

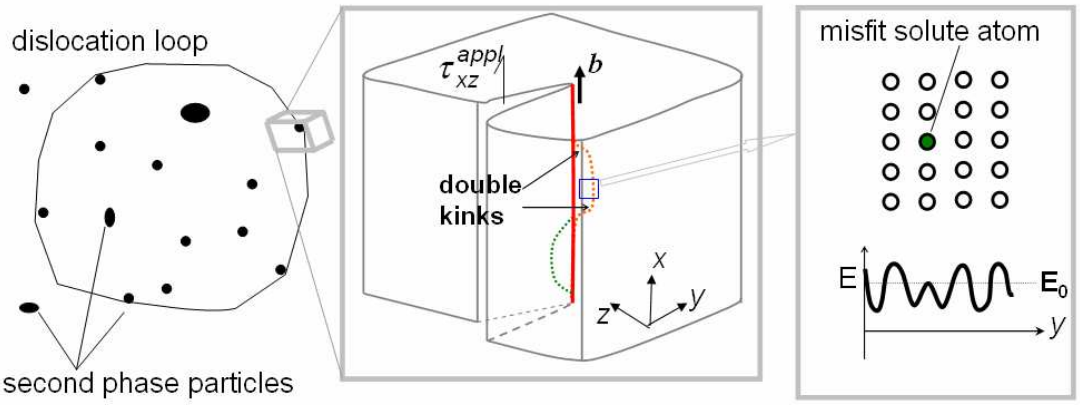

Fig. 1. Dislocation double kink formation model.

2. Models and Governing Equations

2.1 The Model

Consider a metal with dispersed precipitates or solute atoms (see Fig. 1). Figure 1a shows a dislocation loop in a sea of particles. Figure 1b pictures a local double kink and Fig. 1c is a schematic plot of the effect of misfit atom on the periodic Peierls-Nabarro energy. (The derivative of the energy gives the periodic Peierls-Nabarro stress or force.) Obviously, the type of an actual dislocation motion is determined by alloy's micro-nano structure and the interaction between dislocations and particles. Since a curved dislocation loop is formed by a summation of many kinks, its propagation can be characterized by one double kink formation as illustrated in Fig. 1b. The double kink formation along the dislocation loop essentially governs the ductility of the alloy.

Let the Peierls-Nabarro stress magnitude in a crystal be given by [13]:

$$\sigma^{Peierls} = b\frac{\mu}{2c}exp\left(-\frac{\pi a}{c}K\right) \tag{1}$$

where b is Burger vector, K is a constant determined by the second order derivative of interatomic potential, a is the spacing between adjacent slip system, c the lattice

constant along the dislocation motion direction and μ is shear stiffness. Note too that the following expression of Peierls-Nabarro potential *E(y)* has been proposed [13]:

$$E(y) = E_0 - E_p \cos\left(\frac{2\pi y}{c}\right); \qquad E_p = \frac{\sigma^{Peierls} cb}{2\pi} \tag{2}$$

where E_0 and E_p are material constants. The corresponding Peierl-Nabarro stress is given by

$$\tau_{xz} b = \frac{\partial E}{\partial y} \tag{3}$$

For a single crystal with simple cubic structure, in the three dimensional case, the Potential (2) can be written as

$$E(x,y,z) = E_0 - E_p \cos\left(\frac{2\pi x}{c}\right)\cos\left(\frac{2\pi y}{c}\right)\cos\left(\frac{2\pi z}{c}\right) \tag{4}$$

which can be expressed in the form of a Bloch's-like potential:

$$E(x,y,z) = E_0 - E_p \, Re\left\{exp\left[\frac{2\pi x i}{c}\right]\right\} Re\left\{exp\left[\frac{2\pi y i}{c}\right]\right\} Re\left\{exp\left[\frac{2\pi z i}{c}\right]\right\} \tag{5}$$

In this analysis, it is presumed that the inhomogeneities at the two ends of the dislocation line lie along *x*-axis with the same *y* and *z* coordinate in the cubic crystal.

2.2 Governing Equation

A dislocation line ψ in a three-dimensional Cartesian coordinate system can be expressed as:

$$\psi: \quad \begin{cases} x = x \\ y = y(x) \\ z = z(x) \end{cases} \tag{6}$$

As described in [2], the double kink formation in the model of Fig. 1b is equivalent to finding the equilibrium dislocation configuration with the following energy minimum:

$$I(\psi) = \int_{-L}^{L} \left[E(x,y,z)\sqrt{1+\left(\frac{dy}{dx}\right)^2 + \left(\frac{dz}{dx}\right)^2} - \int_0^z \int_0^y \left(\sigma^{misf} + \sigma_{xy}^{appl}\right) b \, dy dz \right] dx \tag{7}$$

and

$$\delta l = 0 \tag{8}$$

Also the dislocation line satisfies the boundary conditions, e.g.

$$y(\pm L) = 0, \quad z(\pm L) = 0 \quad \text{or} \quad y(\pm L) = c_y,\ z(\pm L) = c_z \tag{9}$$

In (7-9) L is the distance between two inhomogenieties which pin the dislocation line; c_y and c_z are constants which are determined the coherency of the inhomogenieties and are adjustable by the variational operation (8); $\sigma^{misf}, \sigma_{xy}^{appl}$ are the misfit-induced stress and external applied stress, respectively; no other stress component is enforced on this field. Also we assume that the stress fields $\sigma^{misf}, \sigma_{xy}^{appl}$ are passive, so the integral within the bracket of (7) with respect to *dydz* along a closed path is path-independent.

2.3 Procedure of Analysis

The governing equation (7-8) will be solved to obtain the equilibrium configuration during double kink formation for the misfit center by alternating the Peierls-Nabarro potential and misfit-induced stress (see Fig. 2). The solution provides quantitative information about the effects of alloying and optimized spacing between particles, which will be used for assisting to establish quantitative correlations among alloying, micro/namo structures, and properties in metallurgical process design.

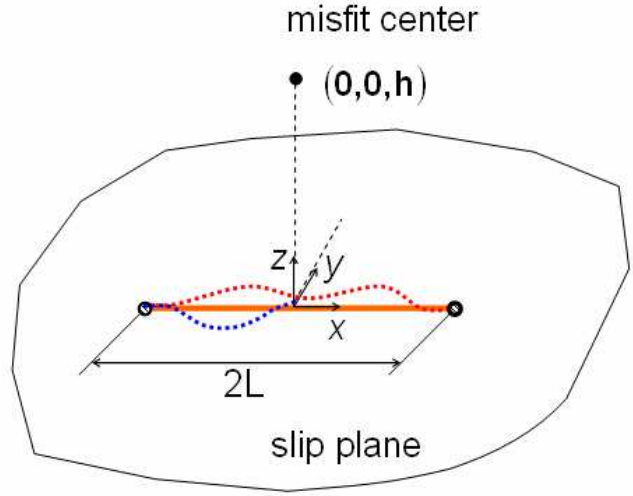

Fig. 2 The problem associated with (7-9) for the misfit center located at (0,0,h)

3. Misfit Analysis

The primary task in solving (7-9) is to find the misfit induced stress field σ^{misf} when alloys additions are added to the Cr matrix. In this analysis the Eshelby's eigen-strain method [14] has been applied to obtain theoretical solution of σ^{misf}, in which the matrix is assumed infinitely large as compared with the particles. The small particles are treated as second phase inclusions with different elastic constants than the matrix and particular details of the particles are ignored (see Fig. 3).

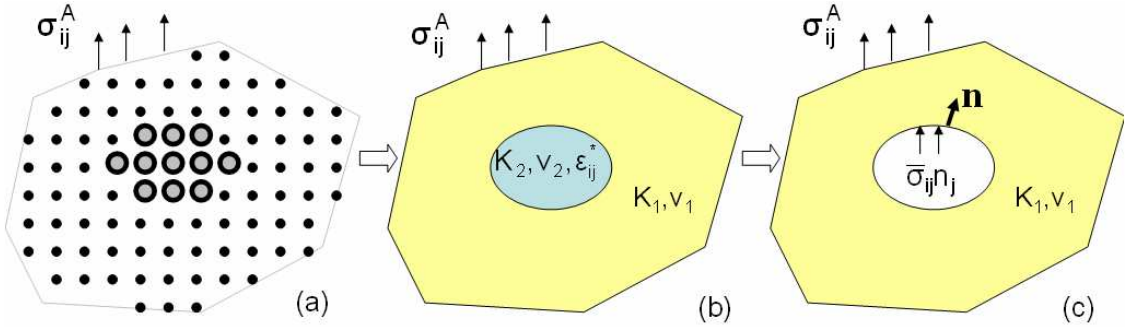

Fig. 3: Analytical model for a matrix with misfit particle/cluster based eigen-strain analysis

3.1 Misfit in Material Properties

The problem associated with the model in Fig. 3 can be stated as (Eshelby [11]): for an infinite isotropic elastic body "I" with bulk modulus K_1 and Poisson's ratio v_1 under a remote uniform applied stress σ_{ij}^A; then, the inclusion "II", which is embedded in "I" with bulk modulus K_2 and Poisson's ratio v_2, will be in the state characterized by an eigen-strain tensor ε_{ij}^* and an corresponding stress tensor $\bar{\sigma}_{ij}$. Under an uniform applied stress σ_{ii}^A, the ε_{ij}^* and $\bar{\sigma}_{ij}$, respectively, are determined by following:

$$\varepsilon_{ii}^* = \frac{3(1-v_1)}{(4v_1-2)K_1-(1+v_1)K_2}\left[(K_2-K_1)\varepsilon_{ii}^A\right] \qquad \varepsilon_{ii}^A = C_{iijj}^I \sigma_{jj}^A \tag{10}$$

and

$$\bar{\sigma}_{ii} = (2\mu_1+\lambda_1)\left(\varepsilon_{ii}^A + S_{iimn}\varepsilon_{mn}^* - \varepsilon_{ii}^*\right) \tag{11}$$

where S_{ijkl} is Eshelby's tensor:

$$S_{ijij}\delta_{ij} = \frac{7-5v_1}{15(1-v_1)}, \quad S_{ijkm}\delta_{ij}\delta_{km} = \frac{5v_1-1}{15(1-v_1)}, \quad S_{ijij}\varepsilon_{ijk} = \frac{4-5v_1}{15(1-v_1)} \tag{12}$$

The bulk modulus is correlated to Young's modulus E by:

$$B = \frac{E}{3(1-2v)}$$

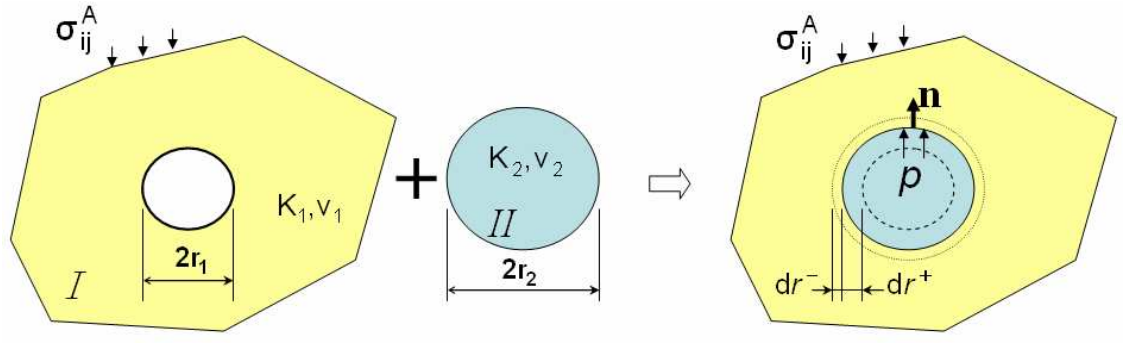

Fig. 4: A model for volumetric misfit analysis

3.2 Volumetric Misfit

Assuming the inclusion to be a sphere that is larger than the void existing in material "I" in Fig. 4. The problem can be described by the Fig. 4 model as an infinite isotropic elastic body "I" with a spherical void with the radius r_1, an inclusion "II" with the radius r_2 which is embedded in "I" and $r_2 \neq r_1$. Hence, misfit-induce radius changes occurs for both the void in "I" and the inclusion. These are denoted as dr^+ and dr^-, respectively, in Fig. 4. The interfacial traction, denoted as *p* (pressure), is determined by the following relation:

$$p = \frac{4\mu_1\mu_2(r_2 - r_1)}{r_1(2\mu_2 + \mu_1(\kappa_2 - 1))} \tag{13}$$

where

$$\kappa = \frac{\lambda + 3\mu}{\lambda + \mu}, \qquad \lambda = \frac{vE}{(1-2v)(1+v)}, \quad \mu = \frac{E}{2(1+v)}$$

The corresponding stresses components are

$$\sigma_{\vartheta\vartheta} = \frac{p}{2}\left(\frac{r_1}{r}\right)^3 \qquad \sigma_{rr} = -p\left(\frac{r_1}{r}\right)^3 \tag{14}$$

4. Results

4.1 Materials Constants

Some materials constants of the metals of interest are listed in Table I:

	Crystal structure at room temperature	Lattice constant (nm)	E (GPa)	*v* Poisson ratio	Ep/b (J/M^2)
Cr	HCP/BCC	0.407/0.291	297	0.21	(BCC)1.44
Re	HCP	0.446	463	0.3	

Ni	FCC	0.352	200	0.31	0.349
V	BCC	0.303	128	0.37	
Fe	BCC	0.287	210	0.297	

4.2 Misfit Induced Stress

Displayed in Fig. 5 are the change of stress (calculated using the equations above) in component delta sigma sub yy along x-axis caused by elastic constants misfit. It is seen the misfit stress increases when either Young's modulus or Poisson's ratio in the inclusion, which is termed "misfit center" in the figure, is larger than that in the matrix. Fig. 6 shows the stress distribution of the volumetric misfit induced stress. A significant stress concentration exist near the inclusion whose amplitude is proportional to the size of the misfit center and is of the order of Young's modulus.

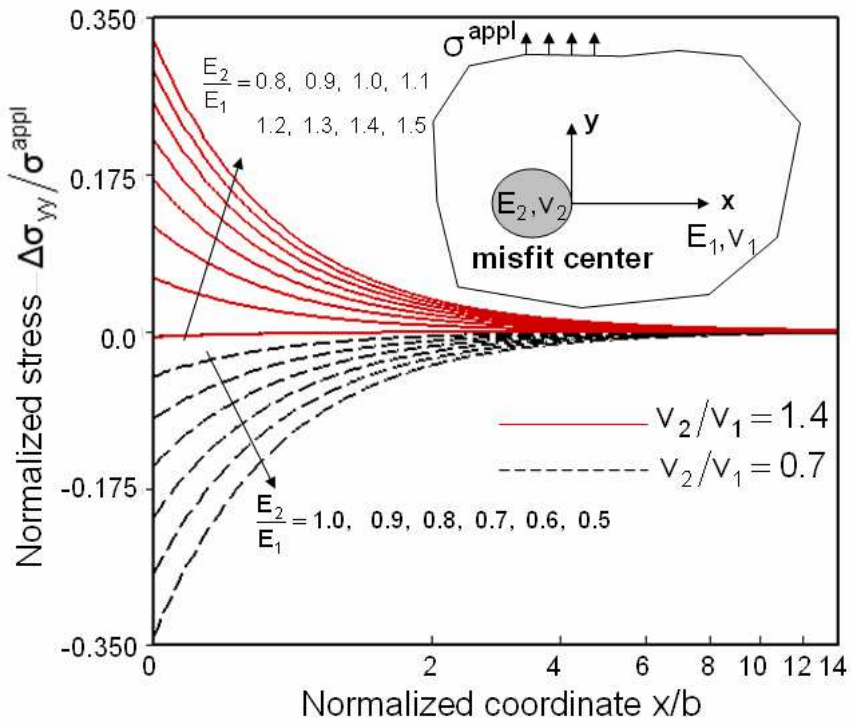

Fig. 5 The change of stress due to elastic constants misfit

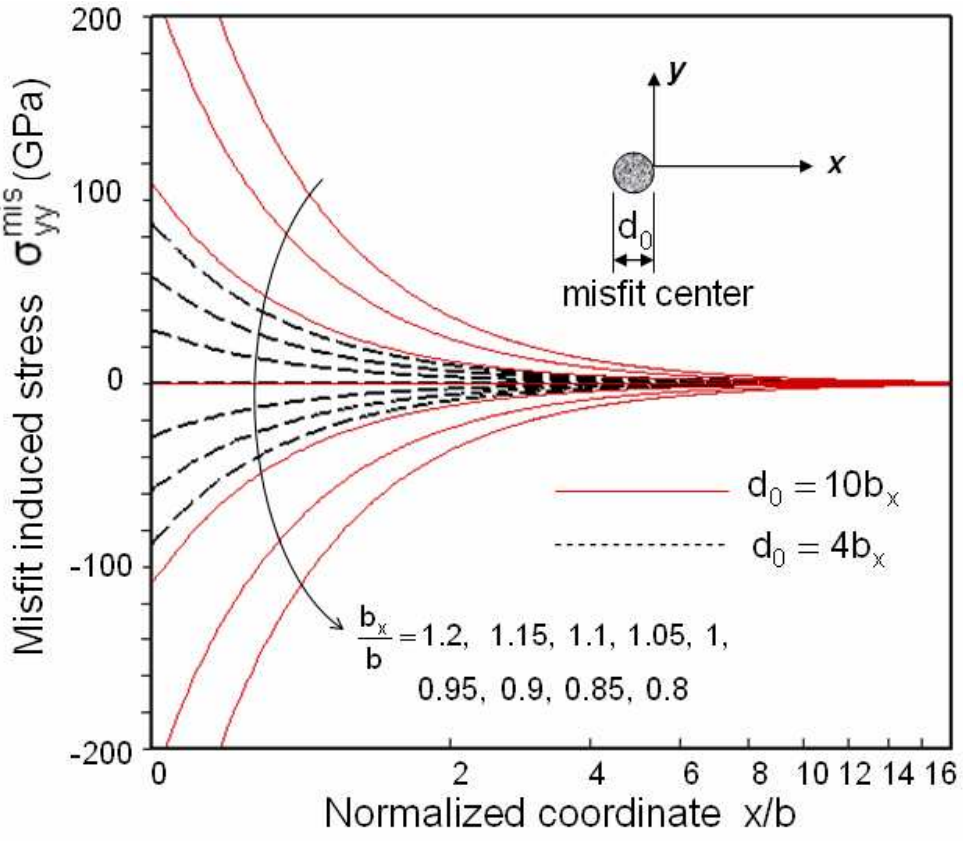

Fig. 6 Distribution of the volumetric misfit induced stress, where b is the burgers vector of the matrix and b_x is that of the misfit center

4.3 Results of Double Kink Formation

The governing equations (7) can be expanded into as following

$$I(\psi) = \int_{-L}^{L} \left[E(x,y,z)Q(x,y,z) - \int_0^z \int_0^y \left(\sigma^{misf} + \sigma_{xy}^{appl} \right) b\,dy\,dz \right] dx \tag{15}$$

where

$$\begin{aligned} G(x,y,z) &= \sqrt{1 + \left(\frac{dy}{dx}\right)^2 + \left(\frac{dz}{dx}\right)^2} \\ &= 1 + \frac{1}{2}\left[\left(\frac{dy}{dx}\right)^2 + \left(\frac{dz}{dx}\right)^2\right] + \frac{3}{2}\left[\left(\frac{dy}{dx}\right)^2 + \left(\frac{dz}{dx}\right)^2\right]^2 + \ldots \end{aligned} \tag{16}$$

Equation (15) has been solved numerically by taking the first two terms of (16) and letting $L = 20b$ and assuming the sum of the derivative terms in (16) is less than unity. Also, the following dimensionless constants are introduced in the analysis:

$$E_R = \frac{E_0}{b^2 \mu}, \quad E_\sigma = \frac{E_p}{b^2 \mu} \tag{17}$$

where E_0 and E_p are the constants in the Peierls-Nabarro potential (1,2); and

$$M_E = \frac{E_x}{E}, \quad M_\upsilon = \frac{v_x}{v}, \quad M_V = \frac{b_x}{b}, \quad \bar{\tau}_{ij} = \frac{\tau_{ij}^A}{\sigma^{Peierls}}, \quad \bar{\tau}_{ij}^{\mu} = \frac{\tau_{ij}^A}{\mu}. \tag{18}$$

Here the subscription "*x*" indicates the materials constants of the misfit center. In (18) the parameter M_V represents the degree of volumetric misfit.

Displayed in Figs. 7-9 are the results when the misfit center lies in the {x,y} plane, i.e, h=0 in Fig.2. Figure 7 shows how the dislocation line "climbs" the Peierls-Nabarro barrier as it decreases or the applied shear stress increases when a very "soft" misfit center is at the middle (which acts as a "void").

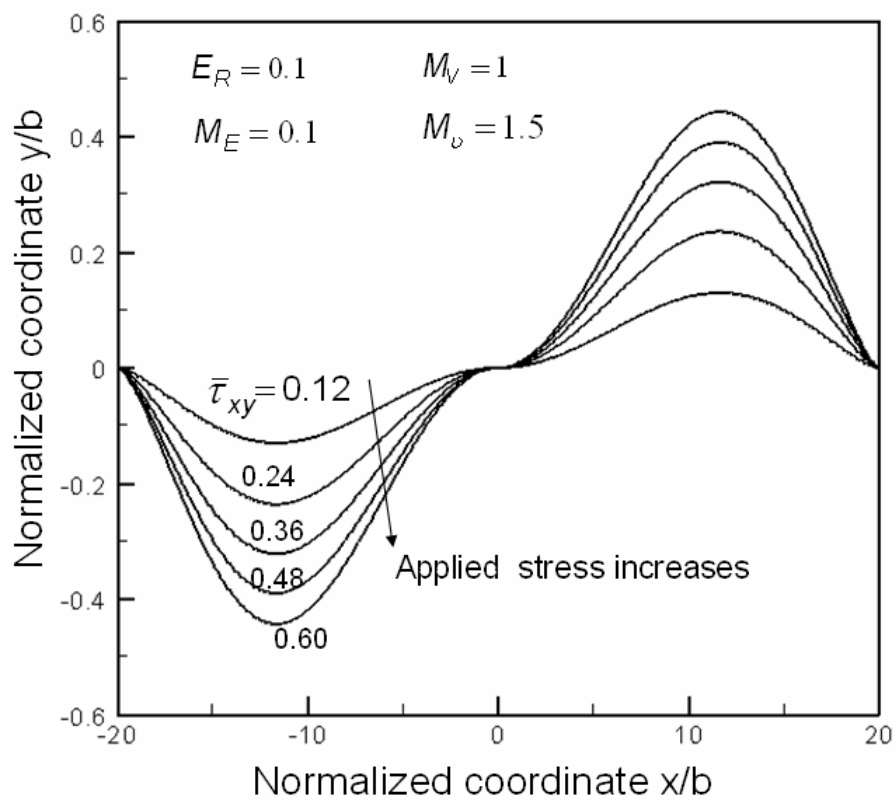

Fig. 7 The dislocation line "climbs" up when applied stress increases

The obtained equilibrium configurations of dislocation lines when a "strong" misfit center exists (due the volumetric misfit) are presented in Fig. 8a,b. These are obtained by

varying the Peierls-Nabarro stress barrier when the applied stress is fixed. Similarly to Fig. 7, the dislocation lines are pinned by the misfit center but two equilibrium solutions can be found for each given materials misfit and applied stress. The first one (Fig. 8a) shows the same trend as that in Fig. 7 but with different scales whereas the second one (Fig. 8b) presents a "Orowan" type curve of a dislocation line hung up on precipitate particles..

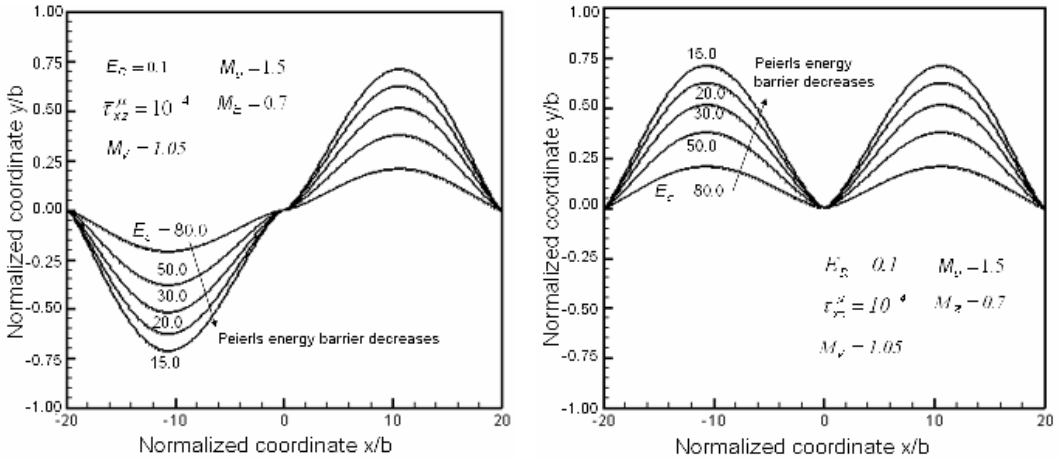

(a) (b)

Fig. 8 Two kinds of equilibrium configurations of the dislocation lines when strong misfit center presents.

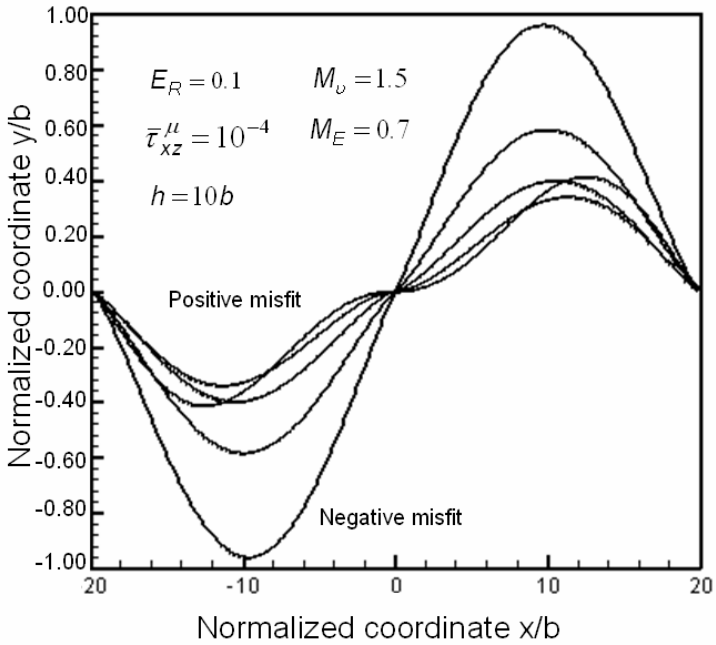

Fig. 9 Two equilibrium configurations of dislocation line when misfit center is away from $\{x,y\}$ plane.

Fig. 9 presents the solutions when *h=10b*, i.e. the misfit center is away from the {x,y} plane, see Fig. 2; where the negative and positive misfit refer to the case $M_V < 1$ and $M_V > 1$, respectively. Although it looks like the negative volumetric misfit is beneficial, the physical meaning in this diagram still needs to be clarified.

Recall the analysis presented in the Section 3 for the misfit analysis associated with Fig. 6. A small lattice constant misfit can cause a huge stress, of the order of Young's modulus. Therefore, a debonding between misfit center and matrix or a dislocation inside the misfit particle may take place. Plotted in Fig. 10 is a graphical analysis, using (10-14), to compute the misfit stress when the displacement caused by the debonding/misfit particle dislocation appears (=1b, 2b, 3b,…), demonstrating that a location-induced displacement can reduce the misfit-induced stress significantly.

By assuming the case of dislocation line touching misfit center to be a permissible solution, the numerical solutions of (7) obtained in this analysis demonstrates that the dislocation line always moves towards to the misfit center at equilibrium. Fig. 11 shows a set of 3D numerical results of (7-9) obtained by varying the distance "h". It presents a "helix-like" topology. This is a favorable dislocation mode and more discussion will be given in the next section.

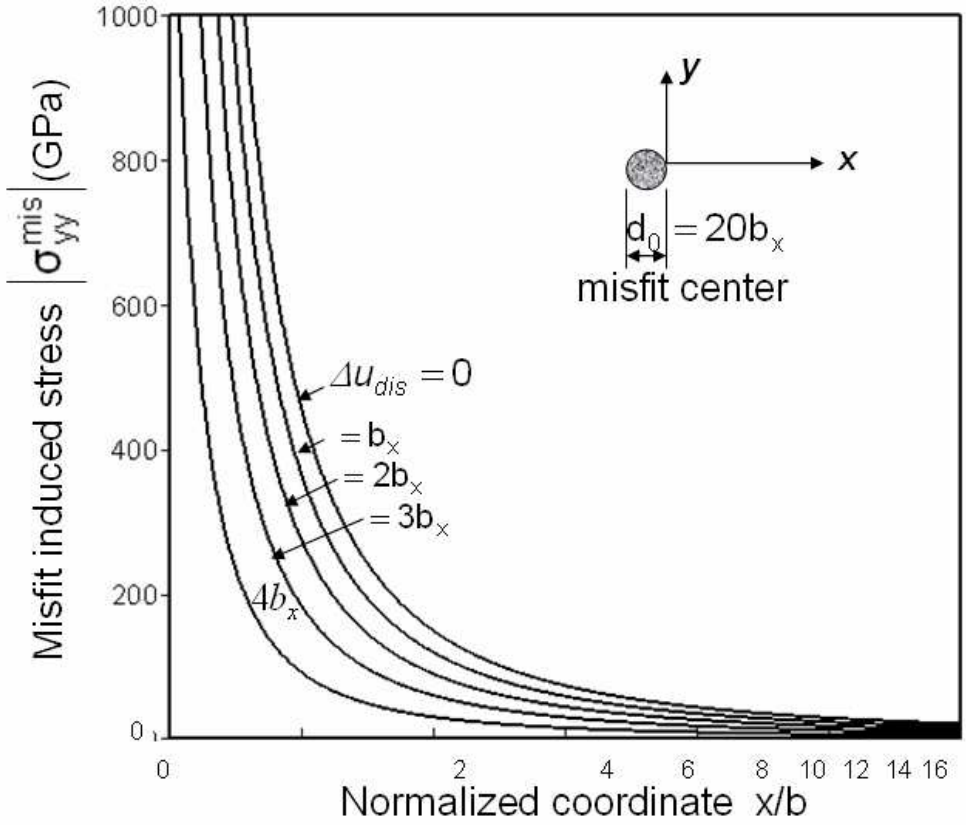

Fig. 10 The variation of misfit-induced stress when a decohesion/dislocation induced displacement, denoted as "Δu_{dis}" in the figure, takes place.

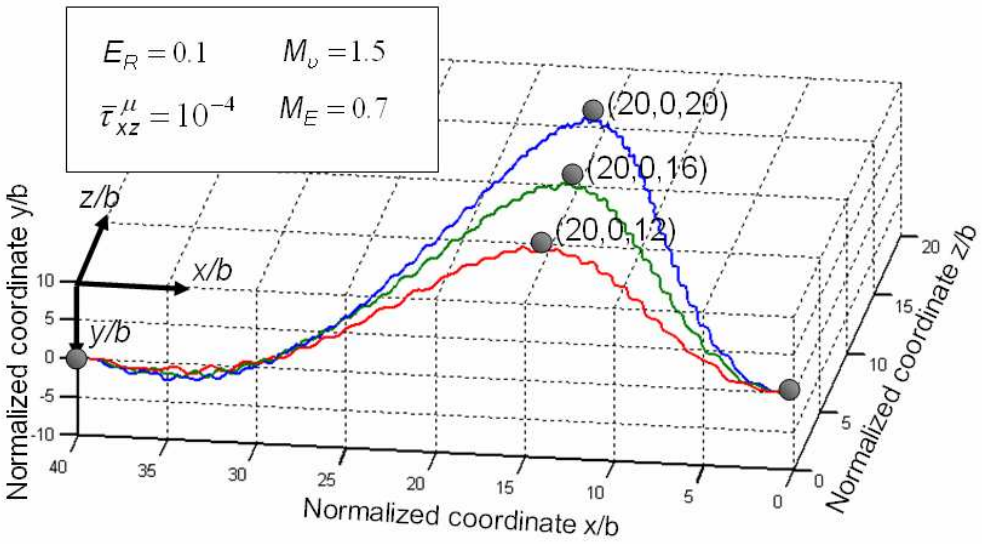

(a)

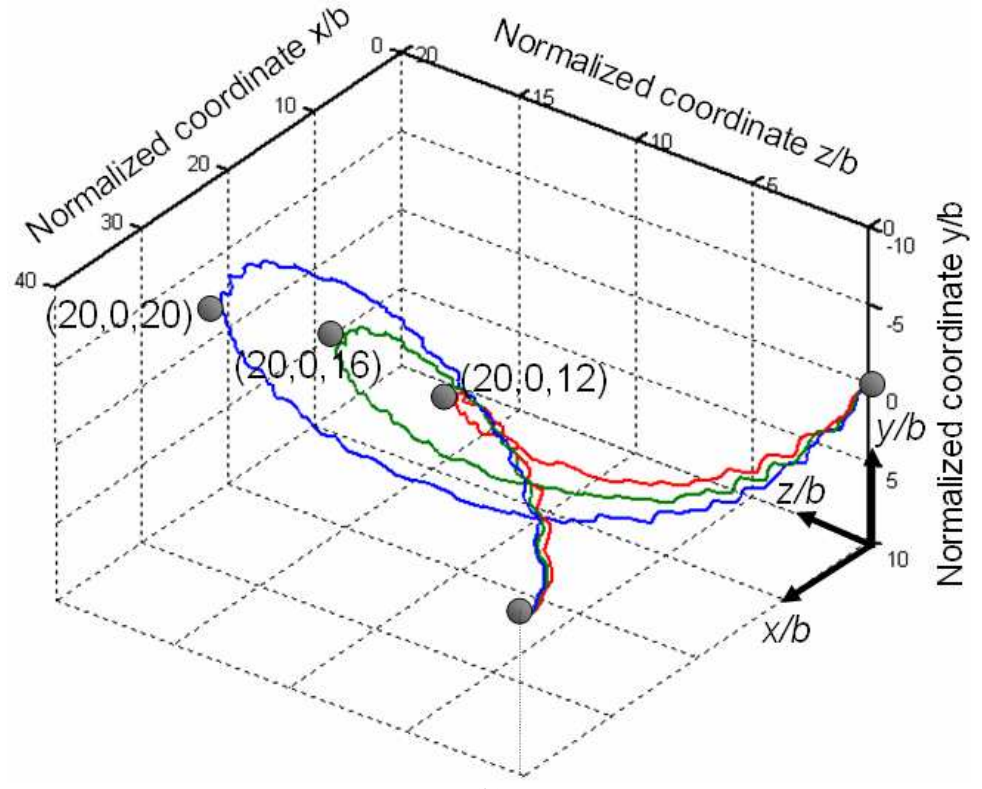

(b)

Fig. 11 Two views of the equilibrium configurations by varying the distance to {x,y} plane, presuming the misfit stress reduction when the dislocation line touches the misfit center

5. Discussion and Conclusions

The analysis in this study reveals that a volumetric and elastic modulus misfit center may result two different dislocation equilibrium configurations, depending upon the position:

(1) When all particles lie in the same slip plane, the major function of these misfit centers is to pin the dislocation line which leads to a precipitation strengthening

(2) The misfit centers locate on different slip plane may result a helix equilibrium configurations of dislocation line when dislocation is easily to be activated in a misfit center

In the study of Mg-based alloys with Li addition, Urakami and Fine [3, 7] indicate that two dislocation motions: basal slip and prismatic slip, may occur in the crystal with close-packed structure such as HCP and BCC. The above mentioned two modes are correlate with these two motions. The precipitate strengthening increases the resistance of basal slip. On the other hand, the zigzag path of a prismatic slip, as the "helical" path demonstrated in Fig. 11, will dissipate more energy than straight slip and induce additional resistance to dislocation motion.

Consider a metal specimen under external load and let the corresponding equivalent stress and strain be denoted as $\bar{\sigma}^{appl}$ and $\bar{\varepsilon}^{appl}$, respectively. The applied load creates dislocation loops within and plastic deformation of the metal. The stress level at which this occurs is termed "intrinsic strength" and is denoted as σ_{th}^{inst} in this paper. Therefore, we can write a criterion for the failure of the metal as below:

$$\bar{\sigma}^{appl} \geq \sigma_{th}^{inst} \tag{19}$$

Based on the analysis introduced in the previous sections, an estimate of the intrinsic strength σ_{th}^{inst} for an alloy with solute/precipitate strengthening/softening, has been suggested as following:

$$\sigma_{th}^{inst} = \sigma_{th}^{matrix} + \Delta\sigma_{th}^{sol} \tag{20}$$

where σ_{th}^{matrix} is the yield strength of the matrix, which is essentially determined by the Peierls-Nabarro stress of the material; and $\Delta\sigma_{th}^{sol}$ represents the contributions of precipitate and solute strengthening/softening.

In an alloy the solute atoms/clusters/precipitates essentially bring up either of the following two opposing functions: smeared Peierls' stress to lower average yielding strength or increased resistance against the motions of dislocation loops. On other hand, as indicated by Figs. 5 an 6, a hard second phase particle or cluster causes high misfit

stress, that can be released through dislocations induced decohesion-debonding around the particle/cluster, see Fig. 10, represented as applied strain induced softening after initial strengthening at macro scale.

Hence, $\Delta\sigma_{th}^{sol}$ can be expressed as the summation of two parts. The first part is relevant to strengthening and predicts a correlation between increment of σ_{th}^{sol} and factors such as the combination of particle strength, dislocation pattern, lattice parameter, solute cluster/precipitate size and spacing. The second part represents the effect of softening. As this study is focused on the latter, we will discuss the issues related to strengthening in details in other report. The expression obtained in [15, 16] is applied but the associated coefficients are modified according to the results obtained in previous secitions:

$$\Delta\sigma_{th-strengthening}^{sol} = \frac{8\beta\left(r_{particle}\right)^2}{Lb}\left(\Delta\sigma_{th}^{particle} - \sigma^{mis}\right) \tag{21}$$

where

β: coefficient, =1 for in-plane dislocation line;

≈ 1.4 for helical dislocation line, e.g, that in Fig. 11.

L: average space between particles

b: Burger's vector

$r_{particle}$: average radius of second phase particle or cluster made of solute atoms

σ_{th}^{matrix}: the flow strength of matrix, which is determined by Peierls-Nabarro barrier.

$\Delta\sigma_{th}^{partilce} = \sigma_{th}^{partilce} - \sigma_{th}^{matrix}$

$\sigma_{th}^{partilce}$: (1) for hard particle, it is the coherent stress at the interface between precipitate particle and matrix,

(2) for solute atom or lose-connected cluster, $\sigma_{th}^{partilce} \approx \sigma_{th}^{solut}$; where σ_{th}^{solut} is the bulk flow strength of the solute atoms.

(3) for soft particle, it's the yield stress of the particles

σ^{mis}: misfit-induced stress

The second part of $\Delta\sigma_{th}^{sol}$ characterizes the effects of solute/precipitate induced softening due to dislocations induced decohesion when applied strain increases, which essentially determines the toughness of a material. According to dislocation theory, e.g. [13], the localized stress near decohesion zone or crack tip can be expressed as

$$\sigma_{tip} \propto \sigma^{appl} n, \qquad n \propto \frac{\sigma^{appl} r_{clust}}{Gb}, \qquad \text{hence: } \sigma_{tip} \propto \frac{r_{clust}}{Gb}\left(\sigma^{appl}\right)^2 \tag{22}$$

where n is the number of dislocation loops and σ^{appl} is applied stress, in the form of equivalent stress. When a fully decohesion-debonding around a particle takes place, the

dislocation loops will be released and this "σ_{tip}" will approach to zero. Hence, an approximation can be made as follows:

$$\Delta\sigma^{sol}_{th-softening} \propto -\sigma_{tip}\frac{L}{k_G b} \tag{23}$$

where k_G is a dimensionless coefficient and the product bk_G is the length scale related to the length of dislocation loop in unit area. By substituting (22) into (23):

$$\Delta\sigma^{sol}_{th-softening} \propto -\frac{r_{clust}L}{Gb^2}\left(\bar{\varepsilon}^{appl}\right)^{2N} \tag{24}$$

where the power hardening/softening law $\sigma^{appl} \propto \left(\bar{\varepsilon}^{appl}\right)^N$ is applied. The relation (24) has been calibrated according to the results obtained in the previous sections and the solution obtained in [15, 16], an expression as following has been obtained

$$\Delta\sigma^{sol}_{th-softening} = -\frac{8\kappa}{\beta}\left(\frac{1-\nu}{2-\nu}\right)\left(\sigma^{matrix}_{th}\bar{\varepsilon}^{appl}\right)^2 \cdot \frac{r_{clust}}{b^2}L \tag{25}$$

where $\bar{\varepsilon}^{appl}$: applied strain, in the form of equivalent strain
κ : a softening coefficient calibrated by numerical computation.

Finally, by combining (22) and (25) we reach:

$$\Delta\sigma^{sol}_{th} = \frac{8\beta}{Lb}\left\{\left(\Delta\sigma^{particle}_{th} - \sigma^{mis}\right)\left(r_{clust}\right)^2 - \frac{\kappa}{\beta^2}\left(\frac{1-\nu}{2-\nu}\right)\left(\sigma^{matrix}_{th}\bar{\varepsilon}^{appl}\right)^2 \cdot \frac{r_{clust}}{b}L^2\right\} \tag{26}$$

The equation (26) reflects the competing mechanisms between strengthening and softening when an alloy is under applied load, which actually provides a prediction of strain softening curve.

Displayed in Fig. 12 is a set of predicted alloy's strain softening curves computed throuogh (26). In this diagram the size and spacing of the second phase particles are fixed ($r_{clust}/b = 9$, $L/b = 60$) whereas the Peierls-Nabarro stress of matrix, i.e. σ^{matrix}_{th}, varies with the fixed ratio: $\Delta\sigma^{particle}_{th}/\sigma^{matrix}_{th} = 0.9$. Since an idealized high strength ductile alloy should possesses an infinite long yielding plateau on the level after fully strengthening, as depicted by the straight line on the top in this diagram, a fast drop of stress with minimum applied strain refers to a brittle behavior of an alloy. As expected, Fig. 12 shows that reducing Peierls-Nabarro stress leads to an increase of ductility, demonstrated by the decrease of strain softening. The gain of ductility is traded off by a deduction of strength. However, by a careful selection of second phase additions (small precipitate particles or solute atoms) with appropriated size and distribution, a desirable dislocation pattern, such as the spiral loops, may result with minimum misfit stress. Under this condition a considerable gain of ductility can be achieved without changing

the Peierls-Nabarro stress, see Fig. 13. In this diagram no misfit stress exists. By increasing the density, i.e. decreasing the spacing, of fine and hard secondary phase particle/cluster, a trend in the improvement in both strength and ductility is revealed.

Based on the theory in [2,6] and expremental observation in [5,9], this analysis leads to a preliminary conclusion that, e.g. for Cr-based alloy system, an equatomic or nearly equatomic solute, i.e. an A_xB_{1-x} binary system where x is about 0.5, may achieve considerable global ductility but with certain amount of reduction in strength. This conclusion can be seen through (26) when $r_{clust} \to b$ and $L \to b$ in this relation. On other hand, in conjunction with non-coplane second (or third) phase-particle with an average diameter 5-10b and spacing $L = 20 - 40nm$, which can achieve strengthening meanwhile trigger double kicks formation with spiral pattern, is a way to gain optimized combination of strength and toughness.

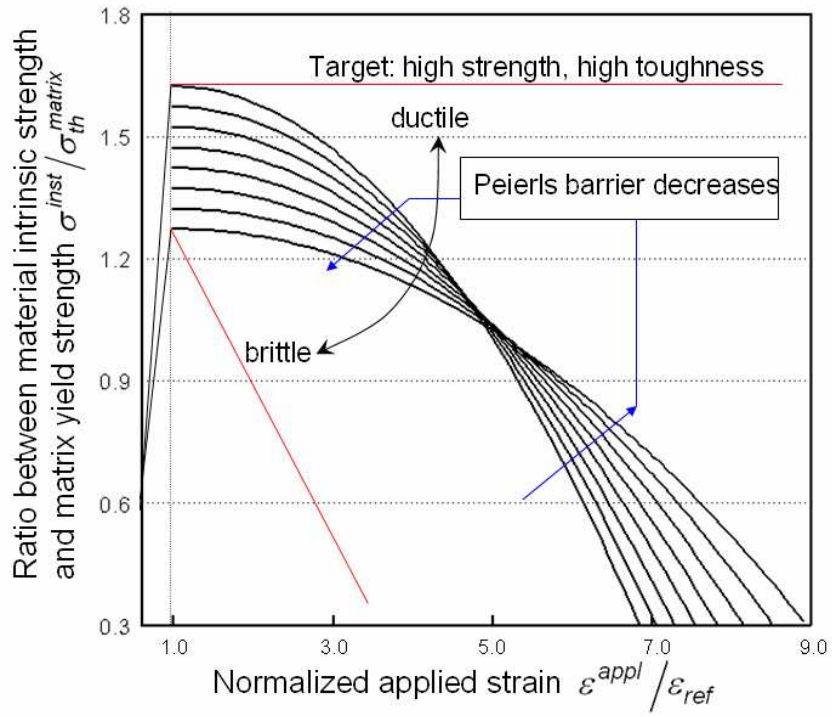

Fig. 12 A diagram of the relationship between Peierls-Nabarro energy barrier and strain softening

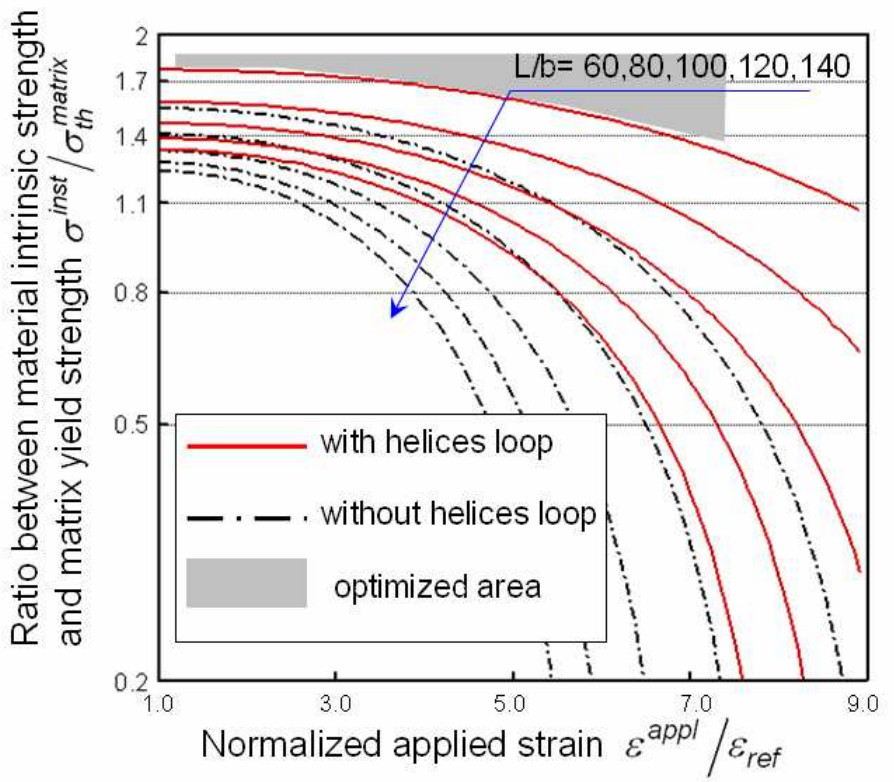

Fig. 13 The effects of the spacing of second phase particles and dislocation loops

Acknowledgement

The authors are pleased to acknowledge the sponsorships of the National Science Foundation Grant No.CMS-0403707.

References

[1] Fine, M.E., Weertman, J., Freeman, A., *Cr-Based Alloys*, a NSF-sponsored project, Northwestern University, 2004.

[2] Weertman, J., *Dislocation Model of Low-Temperature Creep.* Journal of Applied Physics, 1958. **29**(12): p. 1685-1689.

[3] Arsenault, R.J. *Solid solution strenghtening and weakening of bcc solid solutions*. Acta Metallurgica, 1969. **17**(10): p.1291-1297.

[4] Fine, M.E., Tongen A. and Gagliano., *Dinteraction of coherent nanoscale preciptates with screw dislocations to lower the Peierls stress in low carbon steels.* In *Electron Microscopy: Its Role in Materials Science (The Mike Meshii Symposiun).* Edited by J.R. Weertman, M. Fine, K. Faber, W. King and P. Liaw. TMS (The Minerals, Metlas and Materials Society) Warrendale, PA 2003, pp. 229-234.

[5] Urakami, A., Fine, M.E., *Influence of misfit on formation of helical dislocations.* Scripta Metallurgica, 1970. **4**(9): p. 667-672.

[6] Weertman, J, *Mason's dislocation relaxation mechanism*. Physical Review, 1956, **101**(4)**:** p. 1429-1430.

[7] Celli, V., et al., *Theory of Dislocation Mobility in Semiconductors.* Physical Review, 1963. **131**(1): p. 58-&.
[8] Guyot, P. and J.E. Dorn, *A Critical Review of Peierls Mechanism.* Canadian Journal of Physics, 1967. **45**(2P3): p. 983-&.
[9] Urakami, A., PhD Thesis, (Advisor: M.E. Fine), *Effect of Li additions on mechanical properties of Mg based single crystals in basal and prinsmatic sliping*, Northwestern University, Evanston, 1971.
[10] Sato, A., PhD Thesis: *Effect of electron irridation on the strength of iron single crystals*, (Advisor: M. Meshii), Northwestern University: Evanston, 1972.
[11] Freeman, A.J., Full-Potential Linear Argument Plane Wave Code (*FLAPW*) 1991.
[12] Hao, S., Moran, B., Liu, W. K., Olson, G. B., *A Hierarchical Multi-Physics Model for Design of High Toughness Steels.* J. Compute-Aided Materials Design, 2003. **10**(2): p. 99-142.
[13] Weertman, J., Weertman, J. R., *Elementary Dislocation Theory*, 1992, Oxford University Press, Oxford.
[14] Eshelby, J.D., *Elastic inclusions and inhomogeneities*, in *Progress in Solid Mechanics*, I.N. Sneddon, Hill, R., Editor. 1961, North-Holland: Amsterdam. p. 89-140.
[15] J. Fan, S. Hao, "A design-centered approach in developing Al-Si-based light-weight alloys with enhanced fatigue life and strength", **J. Computer-Aided Materials Design,** Volume 11, No. 2-3, Pages 139-161, 2003.
[16] Hao, S., Weertman, J., et al., manuscript in preparation